ABSTRACT

Title of thesis: NO CHANGE IN ENSO HYDROCLIMATE VARIABILITY AFTER THE INDUSTRIAL REVOLUTION AS RECORDED IN δ^{18}O OF *TECTONA GRANDIS L.F.* FROM SOUTHEAST SULAWESI, INDONESIA

Sandy Hardian Susanto Herho, Master of Science, 2023

Thesis directed by: Dr. Michael N. Evans
Department of Geology, University of Maryland College Park

El Niño-Southern Oscillation (ENSO) is a quasi-periodic interannual oscillation of the ocean-atmosphere system in the tropical Pacific which greatly influences global climate variability. However, the long-term response to greenhouse gas forcing is still controversial. In this study, we measured the oxygen isotopic composition of α-cellulose samples at intra-annual resolution from independently crossdated teak cores (*Tectona grandis L. f.*) collected at Muna, Indonesia (5.3ºS, 123ºE, elev. 10m). The site and observation has been previously shown to provide an indirect measure of ENSO activity via local precipitation amount variations associated with ENSO. We created an ensembled composite of the interannual variability for the period 1680-2005 (316 years) using empirical high pass filtering and random sampling of intra-annual resolution measurements. In processing this time series composite, we used Singular Spectrum Analysis (SSA) to high pass filter the data for the interannual variability associated with ENSO. The annually-resolved composite time series of δ^{18}O that we constructed has a higher resolution than other studies that have been

conducted to reconstruct ENSO-hydroclimate activities in the western tropical Pacific region over this period. Using this δ^{18}O composite, we compared the distribution of events in the period before and after the industrial revolution using the two-sample Kolmogorov-Smirnov (KS) test. We found no statistically significant change in the distribution of δ^{18}O anomalies. The same statistical test was applied to the Niño 3.4 reconstruction from the Last Millennium Reanalysis (LMR). The results of this study suggest that if there is indeed a forced response of ENSO, it is as yet indetectable. This may be because the forcing is not yet large enough or the forced response is small relative to the unforced variability. Additional factors that might explain this result in the δ^{18}O composite include its observational and interpretational uncertainty, and in the LMR reconstruction, the scarcity of tropical observational constraints and systematic error in the representation of ENSO in climate simulations.

NO CHANGE IN ENSO HYDROCLIMATE VARIABILITY AFTER THE INDUSTRIAL REVOLUTION AS RECORDED IN δ^{18}O OF *TECTONA GRANDIS L.F.* FROM SOUTHEAST SULAWESI, INDONESIA

by

Sandy Hardian Susanto Herho

Thesis submitted to the Faculty of the Graduate School of the
University of Maryland, College Park in partial fulfillment
of the requirements for the degree of
Master of Science
2023

Advisory Committee:
Dr. Michael N. Evans, Chair/Advisor
Dr. Karen L. Prestegaard
Dr. Raden D. Susanto

Acknowledgments

I am grateful to Austin Carter, Austin Mickels, Cristy Ho, Jenna Wollney, and Mary Gbenro for laboratory support. I also benefitted from helpful discussions with Faiz Fajary, Karen Prestegaard, Michael N. Evans, and R. Dwi Susanto. I also thank Ann Wylie (through the Green Fellowship in Global Climate Change) and Neera Gupta, who partially financed my study at UMD. This study was funded by the NSF grant AGS1903626.

Table of Contents

Chapter 1: Introduction

1.1 Motivation

The El Niño/Southern Oscillation (ENSO) phenomenon produces the most influential impacts on the climate of the tropical Pacific, where it occurs, as well as having far-reaching global consequences [11, 22, 60]. One of the areas that most affected by ENSO is the western equatorial Pacific, since ENSO is a major contributor to the interannual and interseasonal atmospheric convergence and precipitation in this region [50]. While the interannual variability of ENSO under normal conditions (without external radiative forcings) has been extensively studied, it is currently uncertain whether the patterns of its occurrence are significantly affected by external radiative forcing that arise from human activities, such as greenhouses gas (GHG) emissions [16, 17].

1.2 Is ENSO changing? Evidence from climate models

Several studies using climate models indicate an increase in ENSO cold and warm phase event amplitude, suspected to be related to anthropogenic forcing since the industrial revolution [39, 44, 48]. This occurs because of a balance between the release of latent heat in precipitation and radiative cooling in the troposphere [2]. This fact results in an increase in ENSO-driven precipitation in the western equatorial Pacific as a consequence of an increase in GHG emissions. However, the forcing of cold phase events by GHG increases

is small relative to what has been estimated from natural forcings [44]. This ENSO-driven precipitation intensification process in the western equatorial Pacific can be explained by the ocean-dynamical thermostat theory [5, 10, 14, 44]. Increased warming at the surface will have more impact on the western equatorial Pacific than on the eastern equatorial Pacific, this is because warming in the eastern region is offset by the upwelling process. This increase in the SST gradient then exerts an additional force on the pressure gradient which causes the Walker circulation to become stronger, and ultimately increases the SST gradient even more. This mechanism is known as Bjerknes feedback [44]. This finding is still debatable because the consensus results from the simulations of the Coupled Model Intercomparison Project-Phase 3 and 5 (CMIP3 and CMIP5) that the Walker circulation weakens, which will reduce trade winds and make the equatorial thermocline lower, resulting in more "El Niño-like" phenomena [62, 63, 69]. Another study conducted using the Community Earth System Model-Last Millennium Ensemble (CESM-LME) project by Stevenson et al. [59] revealed that the dominant ENSO variability in the last millennium was governed by internal variability. Although there appears to be an increase in ENSO variability in the 20th century, this signal is not robust. However, using the Last Millennium experiments of CMIP5 and Paleoclimate Modelling Intercomparison Project-Phase 3 (PMIP3), Lewis and LeGrande [42] and Hope et al. [37] instead found an increase in ENSO variability in the historical period (1906 - 2005) as a result of an increase in GHG concentrations and land-use changes after the industrial revolution. It can be concluded that there is still debate about how ENSO changes in response to anthropogenic forcings as projected by various climate models after the industrial revolution [17, 32, 41, 72].

1.3 Is ENSO changing? Evidence from paleoclimatology

Additional studies have analyzed paleoclimatic observations and reconstructions of ENSO indicators for changes in properties before and after the anthropogenic increase in radiative forcing of climate, and to establish the range of natural, or unforced variability[e. g. 15, 43, 45, 46, 53, 56]. For example, many study area selections include broad networks of observations [e. g. 43], but are based solely on statistical correlation [e. g. 45] rather than on the forward mechanistic modeling of proxies [e. g. 24]. Others [e. g. 20] are from centers of action for ENSO, but have relatively low reconstruction skill. Leveraging forward modeling of proxies with respect to their environmental controls [26], paleoclimatic data assimilation can be used to update climate model simulations with proxy observations [e. g. 33]. In the approach of Hakim et al. [33] and related studies [73, 74],

$$\mathbf{x}^a = \mathbf{x}^p + \mathbf{K}(\mathbf{y} - \mathcal{H}(\mathbf{x}^p)), \tag{1.1}$$

, where $\mathbf{x}^a$ is the posterior estimate of Niño 3.4 reconstruction, $\mathbf{x}^p$ is the prior estimation from climate simulations, $\mathbf{K}$ is a Kalman gain matrix, $\mathbf{y}$ is the paleoclimatic observations, and $\mathcal{H}$ is the forward operator used to map $\mathbf{x}^p$ to the proxy domain. Note that in this formulation, variance change over time in these products may be convolved with changes associated with observational availability $\mathbf{y}$ over time [e. g. 66]. In the work of Zhu et al. [73, 74], CCSM4-LME simulations [40] were used as the prior, and only coral-based observations and tree-ring records previously shown to record ENSO activity [19, 21, 43] were used for observations. In this study, Zhu et al. [73] found no evidence of an ENSO-mediated response to radiative forcing associated with explosive volcanic events. Historical analysis of gridded SST data, based on dense observations relative to paleoclimatic datasets, together with ENSO modeling suggest no forced response for the period 1856-2003 [12]. Overall,

there does not appear to be consensus from these studies on the anthropogenically forced response to ENSO since the Industrial Revolution. Thus, for the paleoclimatic strategy, it would be beneficial to acquire paleoclimatic data, whose interpretation is underpinned by mechanistic understanding, and which is from key locations in which there is an ENSO-related environmental response, to improve assessments of the sensitivity of ENSO to post-industrial anthropogenic forcing.

1.4 This study

1.4.1 Study location

We addressed this problem by using the annually resolved oxygen isotopic composition of $\alpha-$cellulose ($\delta^{18}O_c$) from teak (*Tectona grandis L. f.*) increment tree cores from Muna, Southeast Sulawesi, Indonesia. These samples were previously and independently dendrochronologically crossdated by D'Arrigo et al. [20] spanning the period 1656-2005 with a sample depth for each year of at least six increment cores per year [49]. The oxygen isotopic composition of cellulose in tree rings in Southeast Asia has been successfully used for reconstructing precipitation and ENSO-driven hydroclimatic responses [51, 58, 68, 75]. Muna is located in in the western equatorial Pacific, known as the Maritime Continent (MC) [52](20°S - 20°N, 90°E - 160°E, Figure 1.1). This area is directly affected by ENSO from a hydroclimatological perspective. Many studies have been conducted that specifically discuss the close relationship between the variability of precipitation over the MC and the ENSO [29, 34, 47, 54, 70]. The negative precipitation anomaly over the MC is considered to have a strong relationship with the ENSO warm phase. The precipitation deficit over the MC is generally associated with a large-scale air mass subsidence anomaly, a weakening of the Walker circulation, and a negative anomaly of sea surface temperature (SST) in the oceans surrounding the MC [54]. Muna is located on the border of region A and region C

in the study of monthly precipitation zone delineation using the double correlation method (DCM) by Aldrian and Susanto [1]. Region A has one peak, as a result of the wet northwest monsoon from November to April, and one trough, which occurs as a consequence of the dry southeast monsoon in the period March to May, in its average annual precipitation pattern. Meanwhile, region C has peak rainfall from June to July and one trough from November to February. Based on the precipitation spectral analysis conducted by Aldrian and Susanto [1], it is known that ENSO has a strong interannual effect on the two regions which are considered to represent the Muna region.

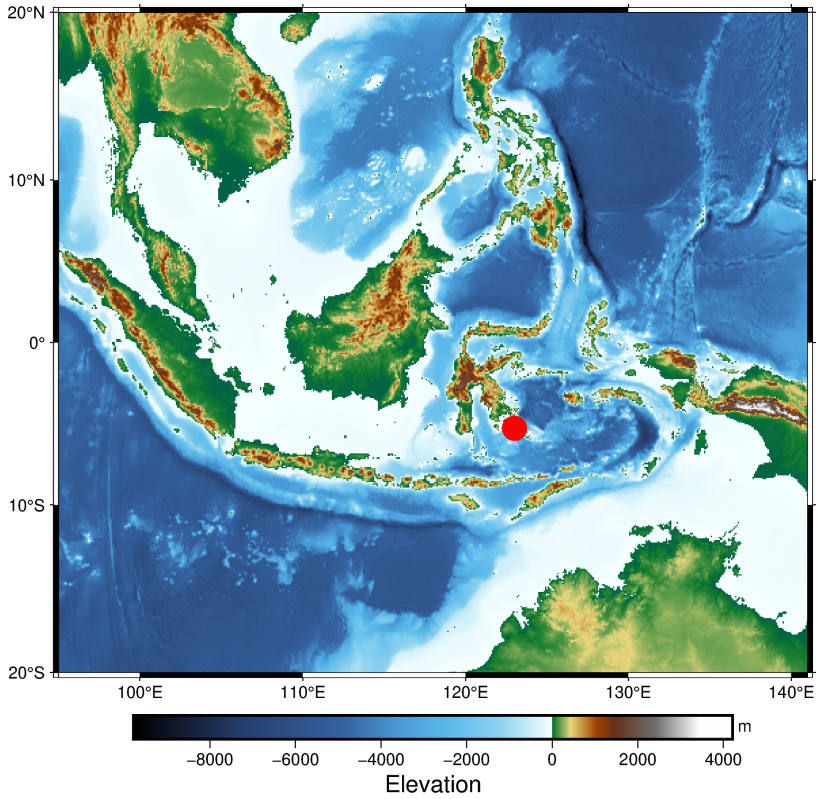

Figure 1.1: Map showing the study location (red dots) in a tropical lowland rain forest (10 m.a.s.l) in the southeastern part of Sulawesi (5.3°S, 123°E).

1.4.2 Data modeling: δ^{18}O of $\alpha-$cellulose

Nurhati et al. [49] used a forward model of $\delta^{18}O_c$ and comparison of simulations with triplicate observations for the period 1971-2005 to show that ENSO-driven precipitation acts as the main control of $\delta^{18}O_c$ in this location. They used the $\delta^{18}O_c$ model of Barbour et al. [4], as modified by Evans [24] for tropical regions,

$$\hat{\delta}^{18}O_c = f\left(T, pr, RH\right) \tag{1.2}$$

, where

- T: monthly average air temperature (°C),
- pr: monthly precipitation (mm),
- RH: relative humidity (%),
- f: forward-deterministic model function as described in Evans [24].

Here, f parameterizes the isotopic composition of precipitation ($\delta^{18}O_p$) as a linear function of precipitation amount, and of atmospheric water vapor ($\delta^{18}O_v$) as a constant value of 8‰ lower than $\delta^{18}O_p$.

$\delta^{18}O_c$ can be modeled deterministically into the following equations,

$$\Delta_c = \Delta_l\left(1 - p_x p_{ex}\right) + \varepsilon_c \tag{1.3}$$

$$\Delta_l = \left\{(1+\varepsilon^*)[1+\varepsilon_k + (\Delta_{wva} - \varepsilon_\kappa \frac{e_s}{e_i}) - 1]\right\}\left(\frac{1-e^{Pe}}{Pe}\right). \tag{1.4}$$

Here, Δ is defined as the oxygen isotopic composition relative to the oxygen isotopic composition of the source water absorbed by plants, which is assumed to be equal to

unmodified $\delta^{18}O_p$. The $(1 - p_x p_{ex})$ fraction of the leaf water isotopic fractionation relative to source water (Δ_l) is an isotope modification caused by the evaporation from leaves and by a partial re-equilibration process between the leaves and unmodified stem water (equation 1.3). The leaf evaporative enrichment (Δ_l) is calculated as a function of the in-situ modified oxygen isotopic composition, temperature-dependent equilibrium and kinetic fractionation factors, and water vapor isotopic fractionation driven by leaf-air differences in specific humidity, modified by the Péclet effect (equation 1.4). Within this model, $\delta^{18}O_c$ is predicted from the oxygen isotopic composition of precipitation, calculated evaporative enrichment at the leaf, partial re-equilibration of leaf water by Péclet back-diffusion, partial re-equilibration of photosynthate with unmodified stem water, and fractionation at cellulose synthesis.

Evans [24] adapted the model from Barbour et al. [4] by parameterizing leaf temperature from air temperature, $\delta^{18}O_p$ as a linear function of precipitation rate, cloud temperature as a linear function of moist adiabatic lapse rate and condensation level, and leaf stomatal conductance as an inverse function of leaf-air saturation vapor pressure deficit, calculable from temperature and relative humidity [24]. Thus, this model can be run with the inputs in equation (1.2).

The temporal correlation between triplicate-observed Muna $\delta^{18}O_c$, and November-April average $\delta^{18}O_c$ simulation, produced from Climate Research Unit (CRU) TS3.01 temperature, precipitation and humidity [35] data at Muna, is statistically significant (1971-2005: $r = 0.36$, $edf = 35$, $p = 0.03$) [49]. As predicted by the $\delta^{18}O_p$ anomalies produced for ENSO events in an isotopically enabled reanalysis of atmospheric climate [71], the observed Muna $\delta^{18}O_c$ record is significantly correlated with the Niño 3.4 index (SST anomalies (averaged over 5°N - 5°S, 170°W - 120°W; 1971-2005, Sep-Oct annual averages: $r = 0.52$, $df = 35$, $p < 0.01$), and the statistically significant pattern correlation of reanalysis $\delta^{18}O_p$ [71] is positive over the MC and negative over the central equatorial Pacific [49], consistent

with climatological understanding of ENSO as described earlier.

1.4.3 Goals of this study

Here we assume that the same mechanistically developed interpretation applies to interpretation of the interannual component of Muna composite $\delta^{18}O_c$ developed for the period extending into the pre-industrial past. By comparative analysis of data for the periods before and after the exponential increase in CO_2 emissions starting in the mid-19th century, we can assess whether there was an associated change in ENSO activity. Specifically, we can test the prevailing hypothesis [7–9] that the probability of ENSO-hydroclimate extremes due to global warming has increased in the industrial period [7–9]. To test the sensitivity of the results and interpretation to uncertainty in the observation and interpretation of the Muna $\delta^{18}O_c$ record, we can perform the same analysis but using as input the independently developed Niño 3.4 index from the Last Millennium Reanalysis "turbo" (LMRt) paleoclimatic data assimilation [73, 74], for which 1941-2000 Niño 3.4 validation $r^2 = 0.62$).

Chapter 2: Materials and methods

2.1 Stable isotope analysis

In this study, we sampled teak (*Tectona grandis L. f.*) increment cores in Muna, Southeast Sulawesi, Indonesia (5.3°S, 123°E) (Figure 1.1) which was dendrochronologically crossdated by D'Arrigo et al. [20]. We analyzed three crossdated samples, tg01gc (1712 - 1995), tg11a (1680 - 1848), and mun6.3 (1798 - 1987). Procedures for preparing samples for isotopic analysis included sample imaging, microtoming, extracting $\alpha-$cellulose, and weighing and wrapping samples in silver capsules. To acquire $\delta^{18}O_c$ data, we thermally converted samples to analyte gas in an elemental analyzer (EA), introduced the analyte into a stable isotope ratio mass spectrometer (IRMS) via a continuous flow interface, collected carbon and oxygen data, and calibrated the data using a 2-point correction for mean and variance to international reference scales [25]. All laboratory work was performed at the Paleoclimate CoLaboratory of the University of Maryland, College Park.

2.1.1 Imaging, intra-annual sampling, and $\alpha-$cellulose extraction

Sample cores were scanned at 1200 dpi to match the core names, orientations, and scales before being separated from their wooden bases. We used a combination of rotary microtome and manual sampling using a razor blade to subsample each crossdated growing season into at least six sequential samples per year. Samples were placed into 1.5 ml centrifuge tubes for $\alpha-$cellulose extraction following a modified Brendel method; a detailed description is

in Anchukaitis et al. [3]. This procedure was done to isolate $\alpha-$cellulose, for which we have a well-developed and tested mechanistic interpretative model (see subsection 1.4.2) [24, 27] from other wood components. This extraction process was carried out by adding nitric acid and acetic acid in a ratio of 1:10 to the sample tubes, then capped sample tubes were heated to 119 - 124°C for 30 minutes. Next, samples were sequentially rinsed with ethanol, then water, then ethanol, then acetone, before being dried at 45°C for 30 minutes. Extracted $\alpha-$cellulose was then stored in a vacuum dessicator for 24 hours or until isotopic analysis. Then each of these dried samples was wrapped and weighted to 200±20 μg or 100±10 μg (depending on the sample size) in a silver capsule to be analyzed for isotopic composition.

2.1.2 $\delta^{18}O_c$ data acquisition

For the analysis of $\delta^{18}O_c$, both samples and standards were run so data could be normalized, allowing drift in the instrument to be accounted for and comparisons to be made with other datasets. Samples and standards were loaded into the autosampler in order, and names and weights were filled into the batch processing file, with care taken to ensure the information matched the order of the samples and standards in the autosampler. The autosampler was then purged with helium to remove any remaining traces of air. Samples were left under helium overnight to make sure they were dry before running the analysis. Once each run was started, C and O from the samples were converted into CO via thermal conversion at 1080°C, and CO_2 and H_2O were removed with an acid/water trap before sample CO was admitted to the IRMS by continuous flow interface. Currents measured for masses 28 ($^{12}C^{16}O$), 29 ($^{13}C^{16}O$), and 30 ($^{12}C^{18}O$) were used to determine isotope ratios. Two independent working standards, SAC ($\delta^{13}C = -25.13 \pm 0.19$ ‰; $\delta^{18}O = 31.0 \pm 0.24$ ‰) and AKC ($\delta^{13}C = -13.80 \pm 0.10$ ‰; $\delta^{18}O = 23.61 \pm 0.24$ ‰) were used for correction

of systematic mean and variance biases introduced by drift and amplitude through each sample batch using scripted functions in MATLAB® [25]. Diagnostic plots were used to check the correction algorithm produced valid corrections. Uncertainty in the isotopic data was estimated as the standard deviation of replicate corrected working standard data across all working standards, and is estimated as 0.4 ‰ averaged across 36 batches of samples and working standards.

2.2 Statistical analysis

2.2.1 Time-series compositing

A compositing step is required to produce an annual unidimensional time series of $\delta^{18}O_c$ based on the three cores of differing time intervals and intra-annual resolutions. The first step was random sampling with replacement of a sub-annual $\delta^{18}O_c$ value from each available annual increment. This step produced 1000 realizations of each of the three time series. We then subtracted each series mean, producing anomaly series, and to high-pass filter for analysis of ENSO-band variations, we used singular spectrum analysis (SSA).

SSA is a nonparametric time-series analysis method which can be implemented on series with missing data [28, 30, 36, 57, 61]. SSA can be divided into two main steps: the decomposition, which consists of embedding and singular value decomposition (SVD), and the reconstruction, which consists of grouping and diagonal averaging [30, 36].

The embedding was implemented for each anomaly realization, a unidimensional series $\mathbf{Y}_N = \{y_1, \cdots, y_N\}$ to be mapped into a multi-dimensional series $\mathbf{X}_1, \cdots, \mathbf{X}_K$, with vector $\mathbf{x}_i = (y_i, \cdots, y_{i+L-1})^T \in \mathbb{R}^L$, where $K = N - L + 1$. The window length L has to satisfy the requirement: $2 \leq L \leq N/2$. The result of this embedding calculation is a trajectory matrix $\mathbf{X}$ with size $L \times K$ which is a Hankel matrix, where all anti-diagonal elements have the same

value, expressed in the following form,

$$\mathbf{X} = \left(\mathbf{x}_{ij}\right)^{L,K} = \begin{pmatrix} y_1 & y_2 & \cdots & y_K \\ y_2 & y_3 & \cdots & y_{K+1} \\ \vdots & \vdots & \ddots & \vdots \\ y_L & y_{L+1} & \cdots & y_N \end{pmatrix}. \tag{2.1}$$

After the embedding calculation, the decomposition step was continued by applying SVD to the trajectory matrix $\mathbf{X}$. We began SVD analysis by defining the covariance matrix $\mathbf{S} = \mathbf{X}\mathbf{X}^T$. Then using the following equation,

$$\det(\mathbf{S} - \lambda\mathbf{I}) \tag{2.2}$$

, we determined the eigenvectors $\mathbf{U}_i$ and their corresponding eigenvalues λ_i. This procedure was followed by constructing a singular value matrix $\mathbf{\Sigma}$,

$$\mathbf{\Sigma} = \begin{pmatrix} \sqrt{\lambda_1} & \dots & 0 \\ \vdots & \ddots & \vdots \\ 0 & \dots & \sqrt{\lambda_L} \end{pmatrix}. \tag{2.3}$$

The principal component matrix is the transpose of the $\mathbf{V}_i$ matrix, which was calculated through the following procedure,

$$\mathbf{V}_i^T = \left(\frac{\mathbf{X}^T\mathbf{U}_i}{\sqrt{\lambda_i}}\right)^T. \tag{2.4}$$

The final result of the SVD is the decomposition of the trajectory matrix $\mathbf{X}$ into eigentriple

as follows,

$$\mathbf{X} = \mathbf{U}_i \mathbf{\Sigma} \mathbf{V}_i^T. \tag{2.5}$$

The matrix $\mathbf{X}_i = \mathbf{X}_1 + \mathbf{X}_2 + \cdots + \mathbf{X}_d$ from the eigentriple was then used to reconstruct the time series through a grouping process by grouping the set of indices $i = \{1, 2, \cdots, d\}$ into a subset of disjoint $I = \{I_1, I_2, \cdots I_m\}$, with $m = d$, so that it could be expanded into this following form,

$$\mathbf{X}_I = \mathbf{X}_{I_1} + \mathbf{X}_{I_2} + \cdots \mathbf{X}_{I_m}. \tag{2.6}$$

The final step to reconstruct the time series based on the power of the spectrum is to perform diagonal averaging. This stage was performed by transforming each matrix in the equation 2.6 into a Hankel matrix to produce the initial time series form as follows,

$$\mathbf{y}_t = \sum_{k=1}^{m} \tilde{y}_t^m, \quad \text{, where } t = 1, \cdots m. \tag{2.7}$$

Because we aimed to do high-pass filtering on each anomaly realization to get interannual variability, we substituted $m = 7$ years and removed $\tilde{y}_1$. The ensemble of 3×1000 high-pass filtered $\delta^{18}O_c$ anomaly timeseries, spanning the entire observational period 1712-1995, were then used to estimate the composite anomaly median and 95th percentile confidence intervals. We implemented all of the time-series compositing processes in the MATLAB® computing environment.

2.2.2 Nonparametric statistical test

The Kolmogorov-Smirnov (KS) test is a nonparametric test of continuous, one-dimensional probability distributions that can be used to compare a sample with a reference probability distribution (one-sample KS test), or to compare two samples (two-sample KS test) [65, 67]. In this study, we used the two-sample KS test. A nonparametric statistical test was used

because it does not assume normality in the time series distribution. The KS test was used to test the null hypothesis that two independent samples come from populations with identical distributions.

- H_0: $F(x) = G(x)$, for all x.
- H_1: $F(x) \neq G(x)$, for at least one value of x.

, where $F(x)$ and $G(x)$ are the cumulative distribution functions (CDFs) of highpassed $\delta^{18}\mathrm{O}_c$ anomalies (hereafter annual $\delta^{18}O_c$ variability) for the population before and after the industrial revolution, respectively. Let $Sn_1(X)$ and $Sn_2(X)$ be the empirical cumulative distribution functions of the $\delta^{18}\mathrm{O}_c$ anomalies before and after the baseline periods, respectively, given by $Sn_1 = k/n_1$ and $Sn_2 = k/n_2$, where k is the same or less than X, and n_1 and n_2 are the number of data points in each observation. The KS statistic is

$$D = \max |Sn_1(X) - Sn_2(X)|. \tag{2.8}$$

To test the sensitivity of the test to definition of the pre-industrial and industrial eras, we used two defensible definitions: (1) 1850 and (2) 1970, defined by the initial point at which anthropogenic greenhouse forcing is estimated to have begun, and the point at which the decadally averaged rate of increase in greenhouse radiative forcing suddenly increased, respectively [72]. We also tested the sensitivity of the results to sample size imbalance by repeating the latter test for independent 25-year time windows before and after 1970. We used the **scipy** library [64] in the Python computing environment for test calculations, and consider $\mathrm{p}_{crit} = 0.05$ for inference. We applied the same test and definitions to the independent December-February (DJF) Niño-3.4 index from the LMRt paleoclimate data assimilation product.[1]

[1]Data available at: https://zenodo.org/record/5893781.ZAqnh3WYXIE.

Chapter 3: Results

There are 1,356 sub-annual measurements of $\delta^{18}O_c$ on tg01c, 788 on tg11a, and 1,048 on mun6.3. Intra-annual resolution $\delta^{18}O_c$ measurements are shown as time series in Figure 3.1. From tg01c, the maximum $\delta^{18}O_c$ is 30.7 ‰ in 1928, and the minimum is 19.3 ‰ in 1765 (Figure 3.1a). From tg11a, the maximum value of $\delta^{18}O_c$ is 28.7 ‰ in 1686, and the minimum value is 22.2 ‰ in 1720 (Figure 3.1b). From mun6.3, the maximum $\delta^{18}O_c$ is 32.2 ‰ in 1981, and the minimum value is 23.0 ‰ in 1934 (Figure 3.1c). The median and 2.5th - 97.5th percentile for each core are shown in Table 3.1 ($\delta^{18}O_c$ values). Series medians differ by almost 2 permil (Table 3.1), and the 95th percentile ranges of values are about 4 ‰, 4 ‰, and 5 ‰, respectively (Table 3.1, $\delta^{18}O_c$ values).

core name	δ^{18}O$_c$		δ^{18}O$_c$ variability	
	median (‰)	[2.5th, 97.5th] (‰)	median (‰)	[2.5th, 97.5th] (‰)
tg01c	25.53	[23.56, 27.52]	0.01	[-1.43, 1.4]
tg11a	25.32	[23.41, 27.27]	0.03	[-1.54, 1.34]
mun6.3	27.33	[24.95, 29.75]	-0.01	[-1.94, 2.22]

Table 3.1: Median and 2.5th - 97.5th percentile confindence limits for each core. Columns 2 - 3 are statistics for the intra-annual δ^{18}O$_c$ series. Columns 4 - 5 are statistics for δ^{18}O$_c$ variability by sample core prior to compositing across cores.

The high pass $\delta^{18}O_c$ composite is shown in Figure 3.2. The solid green line indicates the median values. Meanwhile, the green shaded area shows the 95% percentile interval obtained from 3×1000 randomized realizations. The highest median of the $\delta^{18}O_c$ variability is 1.40 ‰ in 1712, and the lowest is -1.90 ‰ in 1706. The grand median of $\delta^{18}O_c$ variability

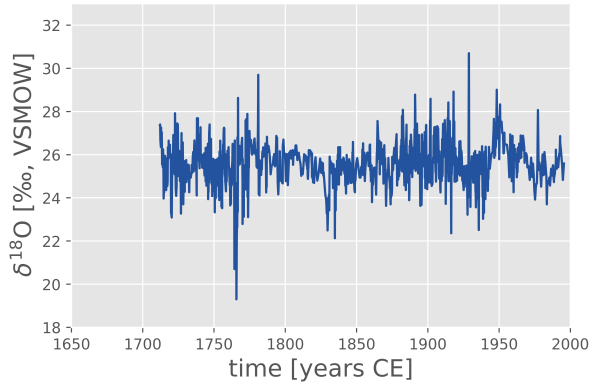

(a)

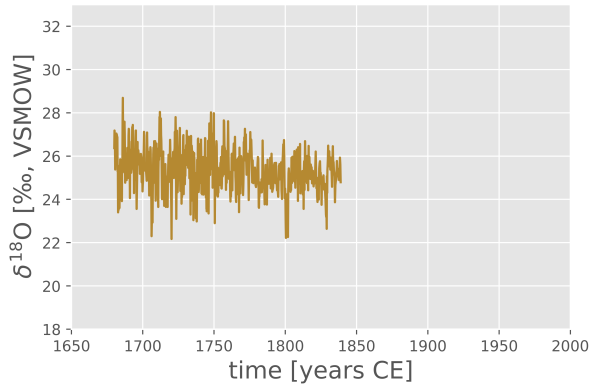

(b)

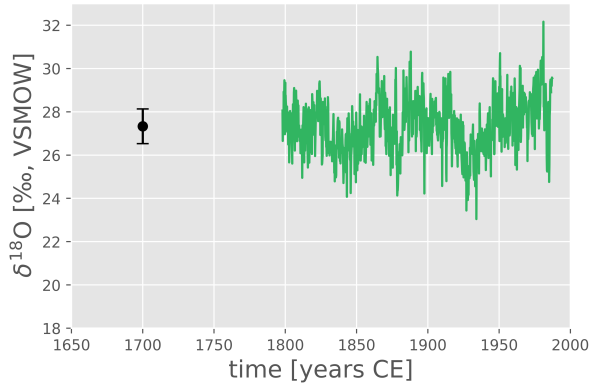

(c)

Figure 3.1: Intra-annual resolution $\delta^{18}O_c$ measurements collected from Muna increment core samples: (a) tg01c, (b) tg11a, and (c) mun6.3. Vertical axis shows oxygen isotopic composition in permil units relative to the Vienna Standard Mean Ocean Water standard (VSMOW), with each scale range = 10 ‰ centered on the median series value. The single point in black at 1700, 27.33 shows observational uncertainty for intra-annual measurement analytical uncertainty, as ±2 standard deviations of the mean of corrected standard measurements. Sequential sample data were assigned sequential dates for Nov of the prior calendar year through April of the following calendar year by linear interpolation; horizontal axis shows time (years CE).

is 0.00 ‰, and the ensemble 95th percentile confidence interval is [-0.98 ‰, 0.88 ‰]. The ensemble $\delta^{18}O_c$ variability is our best estimate of the site composite $\delta^{18}O_c$ record at interannual timescales, sampling observational uncertainty and filtering for mechanistically supported timescales of variation.

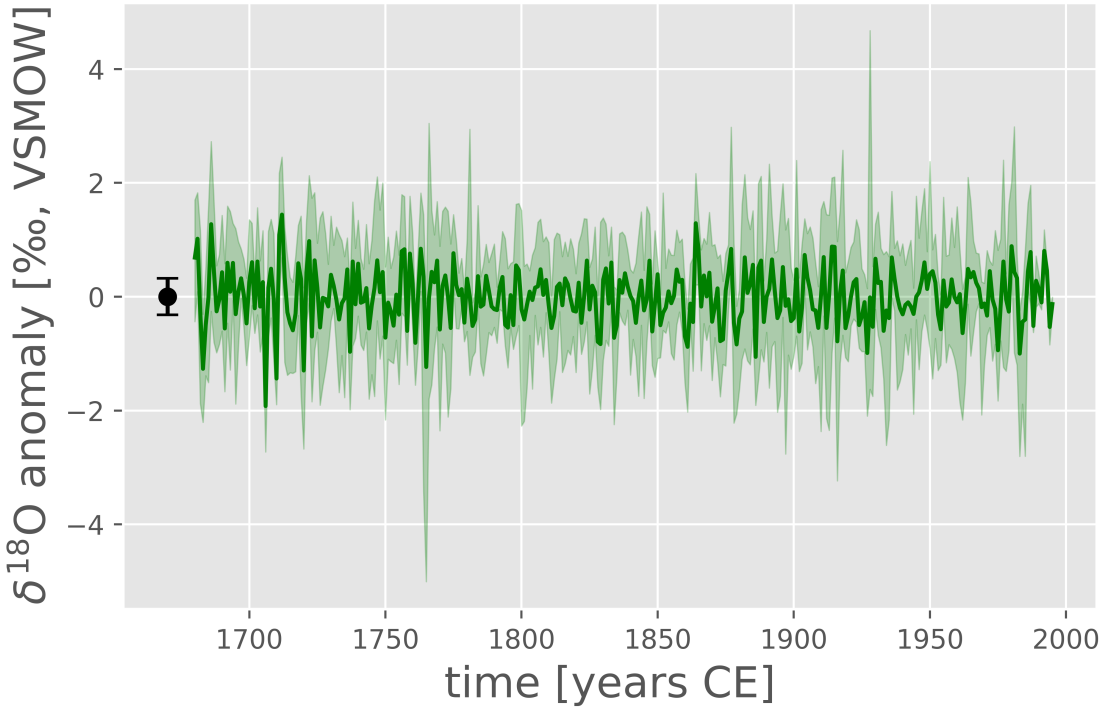

Figure 3.2: $\delta^{18}O_c$ variability composite at annual resolution. Solid green line shows the median, while shaded region denotes the central 95% quantiles from the 3×1000 random realizations. Error bar at point $(0, 1670)$ shows ±2 SE of the observational uncertainty for the annual $\delta^{18}O_c$ variability composite, estimated as $s/\sqrt{n}$, $n = 6$ samples/year, and neglecting the reduction of variance associated with highpass filtering.

The results of empirical CDF calculations of the $\delta^{18}O_c$ variability from the pre- and post-industrial revolution periods are shown in Figure 3.3. Figure 3.3a shows the CDFs of the $\delta^{18}O_c$ variability for the 1680 - 1849 (as the pre-industrial period) and the 1850 - 1995 (as the post-industrial period). Meanwhile, Figure 3.3b shows the CDFs of the $\delta^{18}O_c$ variability for the 1695 - 1969 (as the pre-industrial period) and the 1970 - 1995 (as the post-industrial period). The results of the two-sample KS test showed that there

is no significant difference in the CDFs between the pre-and post-industrial periods, both when the industrial revolution began in 1850 (with statistical values: $D = 0.072$, $p-$value $= 0.780$), or when the industrial revolution began in 1970 (Table 3.2). This result was not sensitive to the choice of SSA embedding dimension for $m = 5, 7, 9, 11$ (Appendix A).

Table 3.2: Statistical results of the two-sample KS test of $\delta^{18}O_c$ anomaly for every 25 years compared to the period after the industrial revolution (1970 - 1995).

period	D_{max}	$p-$**value**
1695 - 1719	0.177	0.733
1720 - 1744	0.142	0.910
1745 - 1769	0.217	0.495
1770 - 1794	0.268	0.233
1795 - 1819	0.226	0.424
1820 - 1844	0.188	0.652
1845 - 1869	0.148	0.882
1870 - 1894	0.137	0.929
1895 - 1919	0.134	0.942
1920 - 1944	0.266	0.241
1945 - 1969	0.257	0.297

As a comparison, we also applied the two-sample KS test to the LMRt DJF Niño 3.4 reconstruction [73, 74] during the same period (1680 - 1995) (Figure 3.4a). Figure 3.4b shows the CDFs in 1680 - 1849 (as the pre-industrial period) and 1850-1995 (as the post-industrial period). Figure 3.4c shows the CDFs in the period 1680 - 1969 (as the pre-industrial period) and 1970-1995 (as the post-industrial period). Based on the *a-priori* $p = 0.05$ critical level, we infer that there is no significant difference between the CDFs for the periods 1680 - 1849 and 1850 - 1995, with statistical values: $D = 0.140$ and $p-$value $= 0.082$ (Figure 3.4b). We make the same inference if the industrial revolution period is defined to start in 1970 (Table 3.3, Figure 3.4c).

Table 3.3: Statistical results of the two-sample KS test of Niño 3.4 reconstruction for every 25 years compared to the period after the industrial revolution (1970 - 1995).

period	D_{max}	$p-$**value**
1695 - 1719	0.345	0.060
1720 - 1744	0.346	0.059
1745 - 1769	0.228	0.413
1770 - 1794	0.268	0.233
1795 - 1819	0.305	0.128
1820 - 1844	0.268	0.233
1845 - 1869	0.305	0.128
1870 - 1894	0.300	0.147
1895 - 1919	0.285	0.216
1920 - 1944	0.331	0.098
1945 - 1969	0.337	0.079

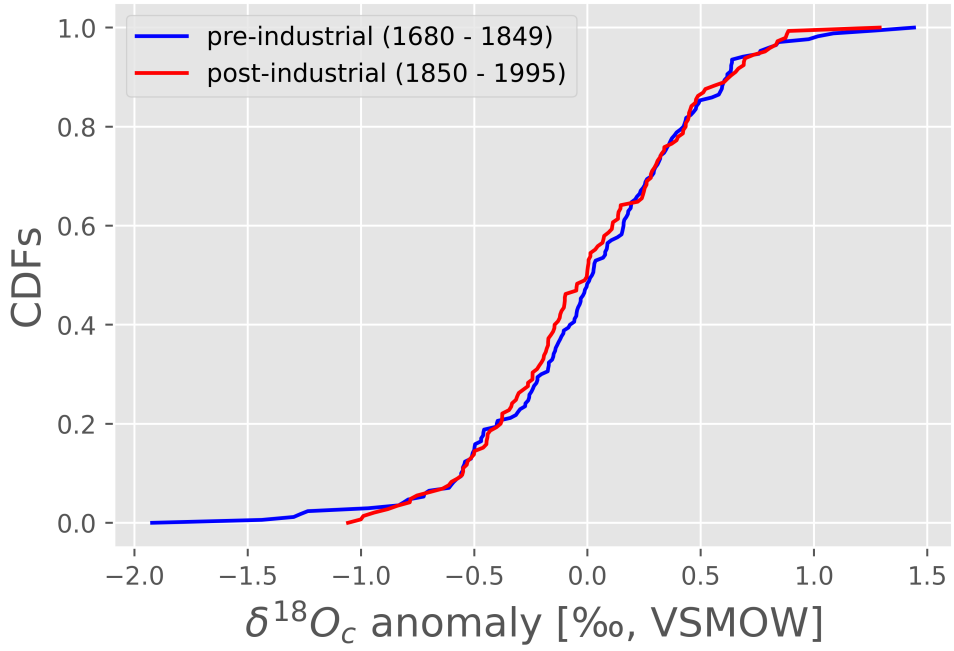

(a)

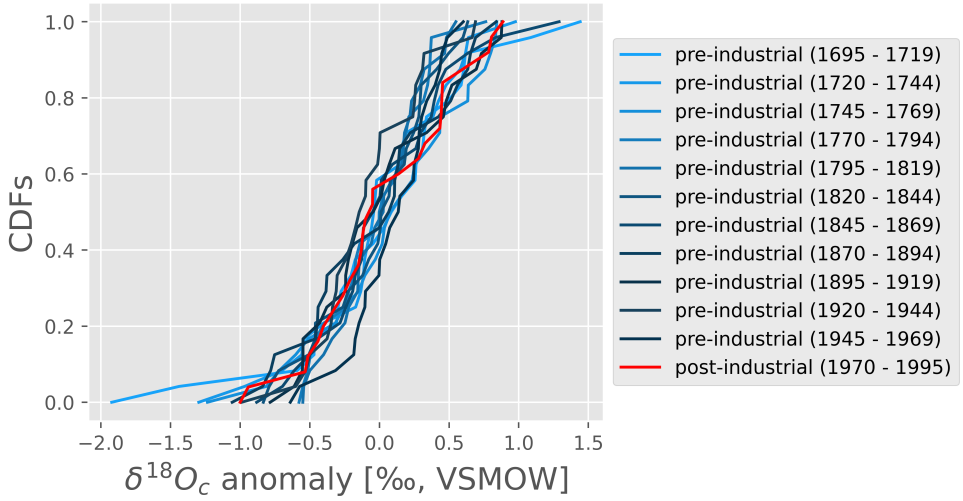

(b)

Figure 3.3: Empirical cumulative probability density function (CDF) curves of the annual $\delta^{18}O_c$ variability. The red line shows the period after the industrial revolution, while the blue lines show the periods before the industrial revolution. We used two different definitions of the anthropogenic era to show that the results are not sensitive to its definition of the beginning of the exponential increase in the anthropogenic forcings. In (a) the industrial revolution began in 1850, while in (b) the industrial revolution began in 1970.

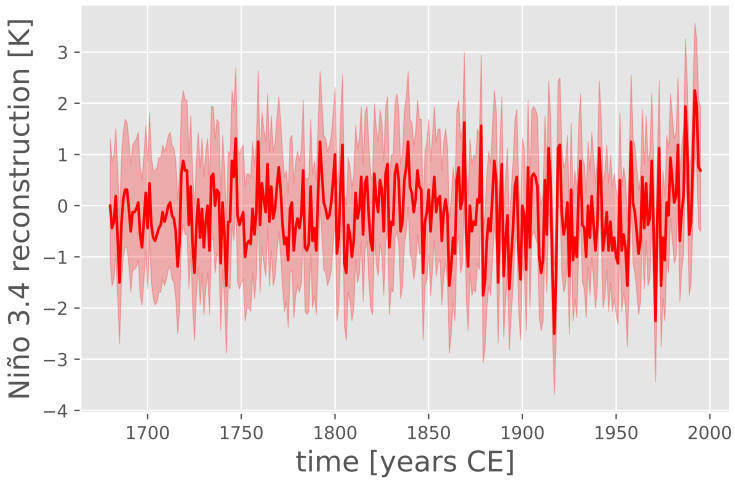

(a)

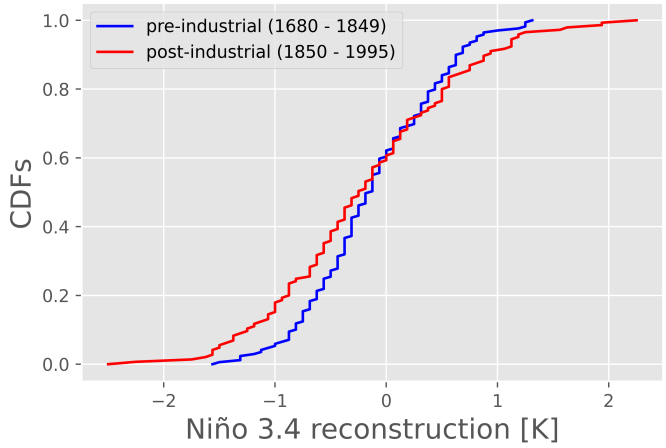

(b)

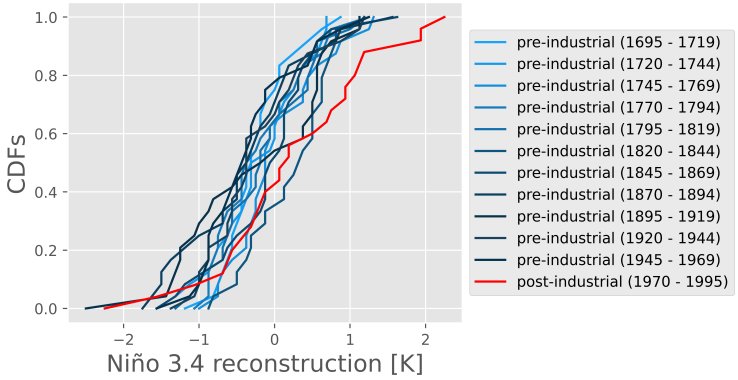

(c)

Figure 3.4: (a) DJF Niño 3.4 reconstruction (1680 - 1995) using the LMR turbo (LMRt) framework [74] from the analysis of Zhu et al. [73], solid red line shows median values; shaded area denotes the 95% quantiles. (b - c) same as the Figure 3.3, but for the LMR data.

Chapter 4: Discussion

4.1 Summary of results

We constructed an annually resolved site composite record from three temporally overlapping, intra-annually resolved $\delta^{18}O_c$ series. Based on prior work demonstrating a link to ENSO activity on interannual timescales, we infer no change in the inferred distribution of ENSO events through the 316 year (1680-1995) composite record. This result is sensitive to neither the parameters in data compositing and highpass filtering, nor the choice of startpoint of significant greenhouse gas radiative forcing as either 1850 or 1970. Our study shows no difference in ENSO variability as a result of changes in anthropogenic forcings regardless of the initial period of the exponential increase.

4.2 Comparison with prior studies

Our results are independently replicated by reaching the same inference from analysis of LMRt Niño-3.4 index reconstructions for the same intervals. However, we also find that in these results, some intervals give significances that are only slightly above the canonical statistically significant $p-$value ($p < 0.05$) (Table 3.3, Figure 3.4b, c). This result, which is most apparent for the 17th and 20th centuries (Table 3.3), may be due to artifacts in the LMR product. Historical observations [12][1] do not support the $\approx 1^o$C warming in the

[1] https://iridl.ldeo.columbia.edu/SOURCES/.Indices/.nino/.EXTENDED/.NINO34/figviewer.html?plottype=line.

reconstructed Niño 3.4 index. One factor that might explain the 17th century change in distribution could be the tendency of data assimilation products to resolve less variance as observational coverage decreases. For the spurious 20th century warming and associated change in distribution of Niño3.4 anomalies, we speculate that the forward operators used in the data assimilation may have transformed a calibration period trend into a reconstructed warming. Alternatively, this trend could arise from biased representation of ENSO, or the response of ENSO to radiative forcing, in the CCSM4-LME simulations. Further investigation is needed, both statistically (e.g. by using the False Discovery Rate (FDR) [18]) and dynamically (e.g. by correcting the cold tongue bias representation of the input model used in the LMRt framework [31]), to address this issue. Our findings do differ from the those of Liu et al. [45]. In their analysis of $\delta^{18}O_c$ observations from Taiwan for 1190-2007 CE, they inferred an increase in ENSO variability at the end of the 20th century. However, Liu et al. [45] did not test statistical significance of variance changes in their study.

Chapter 5: Conclusion

Our inference is consistent with most studies of paleo ENSO since the Pliocene, which suggests that the external radiatively forced response of ENSO may be small relative to the unforced internal variability [23]. This conclusion is provisional because there are considerable uncertainties in the observations, reconstructions and modeling of ENSO and its forced response. Nurhati et al. [49] showed that the interpretation of the Muna composite $\delta^{18}O_c$ variability record explains less than 1/3 of the interannual variance associated with ENSO, and the Muna record is from only one location. Further confidence can be developed from paleoclimatic data assimilation, but products such as LMRt also have uncertainties associated with data modeling, changes in observational coverage over time, and biases in the prior climate states used. Finally, there is as yet no model consensus on the forced response of ENSO. At present, the evolution of ENSO amplitude, frequency, and variability of anthropogenic forcings is still poorly constrained, and there is no inter-model consensus on projected changes in the dynamics of ENSO diversity in response to the exponential increase in GHG since the industrial revolution [6, 13, 17]. A more in-depth physical investigation is needed on the relationship of anthropogenic forcings to changes in ENSO variability, for instance concerning ENSO diversity, represented by Central Pacific (CP) and Eastern Pacific (EP) events [38].

Historical observations suggest a high degree of inter-event variations from the mid-19th century to the present, consistent with what an intermediate compexity ENSO forecast model might produce without anthropogenic forcings [12]. Paleoclimatic observations

and reconstructions extend this result further into the pre-anthropogenic past, but their analysis fails to disprove the hypothesis that the forced signal, if present, is difficult to detect within the large spread of the natural variability. Such efforts will be improved by the establishment of more high resolution observations in other ENSO-sensitive regions, such as equatorial South America [55], data modeling, and the further development of spatially resolved data assimilation products. Until either the climate simulations produce a clearer consensus, and actual radiative forcing and observed variability exceeds the historical and paleoclimatogically observed or reconstructed envelope, the effect of anthropogenic forcings on ENSO variability will remain unclear.

Appendix A: Statistical analyses for other embedding dimensions of the high-pass filtered time series

To test that the computational results of our high-pass filtered time series are not sensitive to the arbitrary embedding dimension (m = 7), we performed high-pass SSA filtering with m = 5, 9, and 11. The results are shown in Figure A.1. After extracting $\delta^{18}O_c$ variabilities with different embedding dimensions, we applied the two-sample KS test as we did in subsection 2.2.2. Empirical CDFs for m = 5, 9, and 11, respectively shown in Figures A.2, A.3, and A.4. KS test results comparing CDFs (for m = 5, 9, and 11) in 1680 - 1850 with 1850 - 1995 are shown in Table A.1. The results of the KS tests for the post-1970 period for m = 5, 9, and 11 are shown in Tables A.2, A.3, and A.4, respectively. The KS tests with these different embedding dimensions show no statistically significant differences ($p < 0.05$) between $\delta^{18}O_c$ variabilities before and after the industrial revolution.

Table A.1: Statistical results of the two-sample KS test of $\delta^{18}O_c$ variabilities ($m = 5, 9, 11$) for 1680 - 1849 compared to the period after the industrial revolution (1850 - 1995).

embedding dimension (m)	D_{max}	$p-$**value**
5	0.061	0.91
9	0.078	0.688
11	0.091	0.487

Table A.2: Statistical results of the two-sample KS test of $\delta^{18}O_c$ variability (m = 5) for every 25 years compared to the period after the industrial revolution (1970 - 1995).

period	D_{max}	$p-$**value**
1695 - 1719	0.138	0.923
1720 - 1744	0.178	0.721
1745 - 1769	0.218	0.483
1770 - 1794	0.191	0.627
1795 - 1819	0.226	0.424
1820 - 1844	0.186	0.664
1845 - 1869	0.111	0.987
1870 - 1894	0.138	0.923
1895 - 1919	0.092	0.999
1920 - 1944	0.226	0.424
1945 - 1969	0.302	0.140

Table A.3: Statistical results of the two-sample KS test of $\delta^{18}O_c$ variability (m = 9) for every 25 years compared to the period after the industrial revolution (1970 - 1995).

period	D_{max}	$p-$**value**
1695 - 1719	0.137	0.929
1720 - 1744	0.143	0.904
1745 - 1769	0.142	0.910
1770 - 1794	0.228	0.413
1795 - 1819	0.226	0.424
1820 - 1844	0.225	0.436
1845 - 1869	0.143	0.904
1870 - 1894	0.132	0.947
1895 - 1919	0.172	0.766
1920 - 1944	0.305	0.128
1945 - 1969	0.189	0.640

Table A.4: Statistical results of the two-sample KS test of $\delta^{18}O_c$ variability (m = 11) for every 25 years compared to the period after the industrial revolution (1970 - 1995).

period	D_{max}	$p-$**value**
1695 - 1719	0.112	0.985
1720 - 1744	0.143	0.904
1745 - 1769	0.103	0.994
1770 - 1794	0.225	0.436
1795 - 1819	0.223	0.448
1820 - 1844	0.192	0.616
1845 - 1869	0.143	0.904
1870 - 1894	0.209	0.554
1895 - 1919	0.135	0.936
1920 - 1944	0.343	0.063
1945 - 1969	0.228	0.413

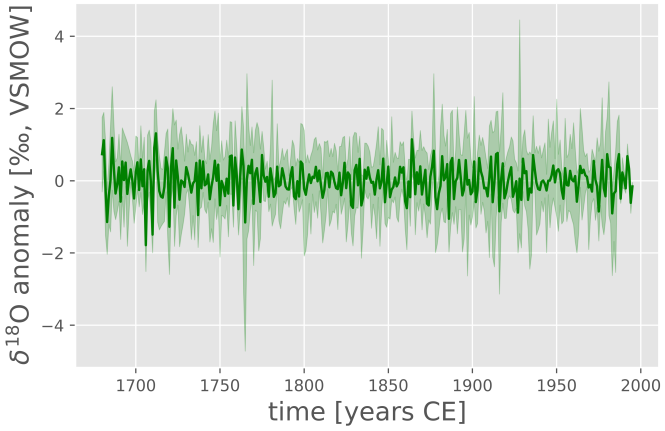

(a)

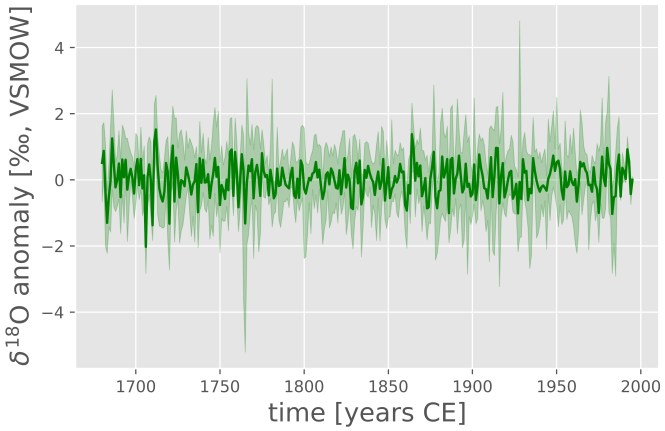

(b)

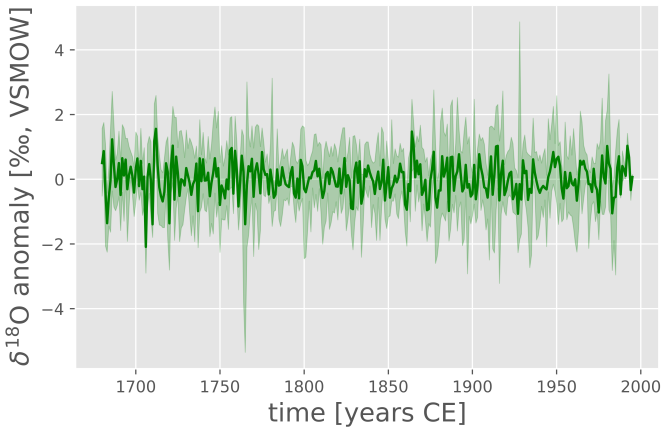

(c)

Figure A.1: Annual $\delta^{18}O_c$ variability. Solid green line shows the median, while shaded region denotes the central 95% quantiles from the 3×1000 random realizations for (a) $m = 5$, (b) $m = 9$, (c) $m = 11$.

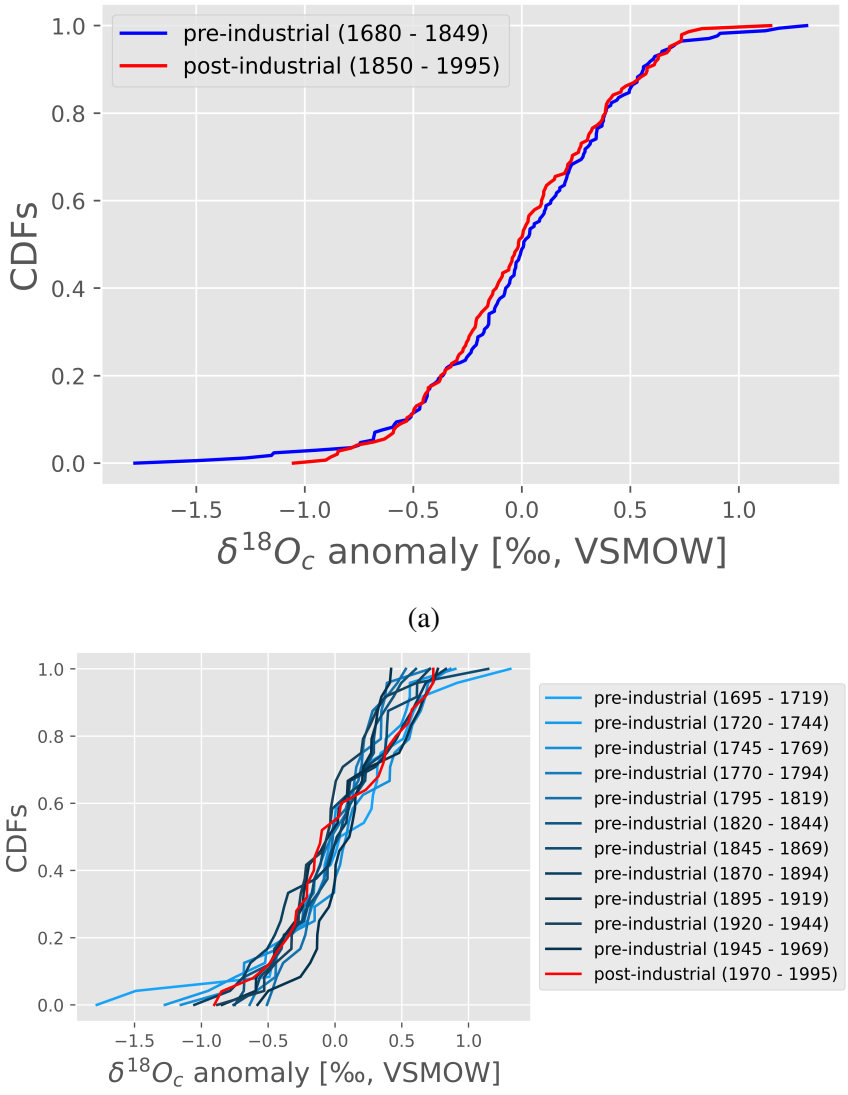

Figure A.2: Empirical cumulative probability density function (CDF) curves of the annual $\delta^{18}O_c$ variability (high-pass filtered $m = 5$). The red line shows the period after the industrial revolution, while the blue lines show the periods before the industrial revolution. We used two different two different definitions of the anthropogenic era to show that the results are not sensitive to its definition of the beginning of the exponential increase in the anthropogenic forcings. In (a) the industrial revolution began in 1850, while in (b) the industrial revolution began in 1970.

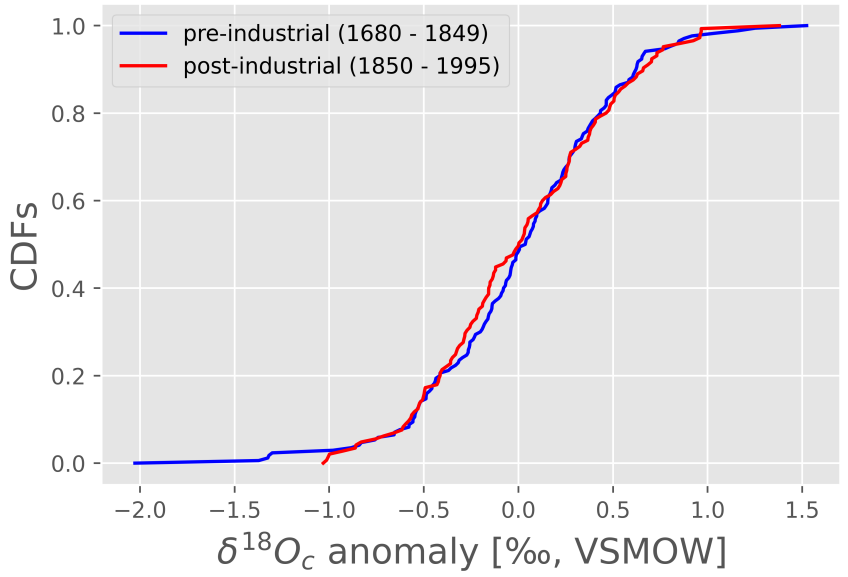

(a)

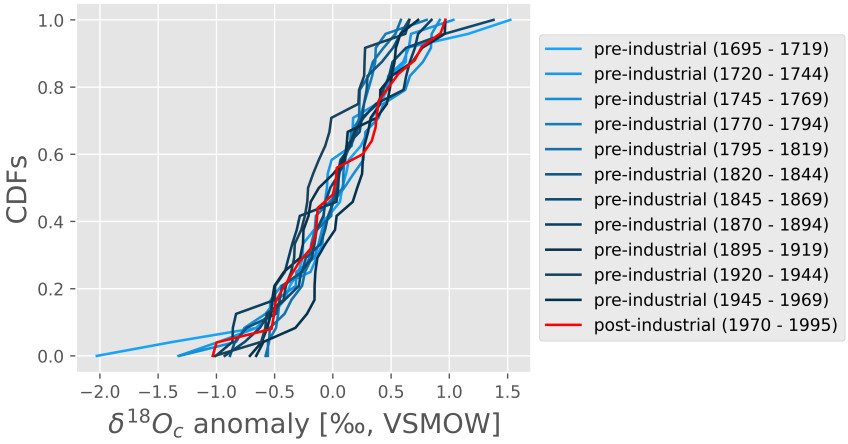

(b)

Figure A.3: Empirical cumulative probability density function (CDF) curves of the annual $\delta^{18}O_c$ variability (high-pass filtered $m = 9$). The red line shows the period after the industrial revolution, while the blue lines show the periods before the industrial revolution. We used two different definitions of the anthropogenic era to show that the results are not sensitive to its definition of the beginning of the exponential increase in the anthropogenic forcings. In (a) the industrial revolution began in 1850, while in (b) the industrial revolution began in 1970.

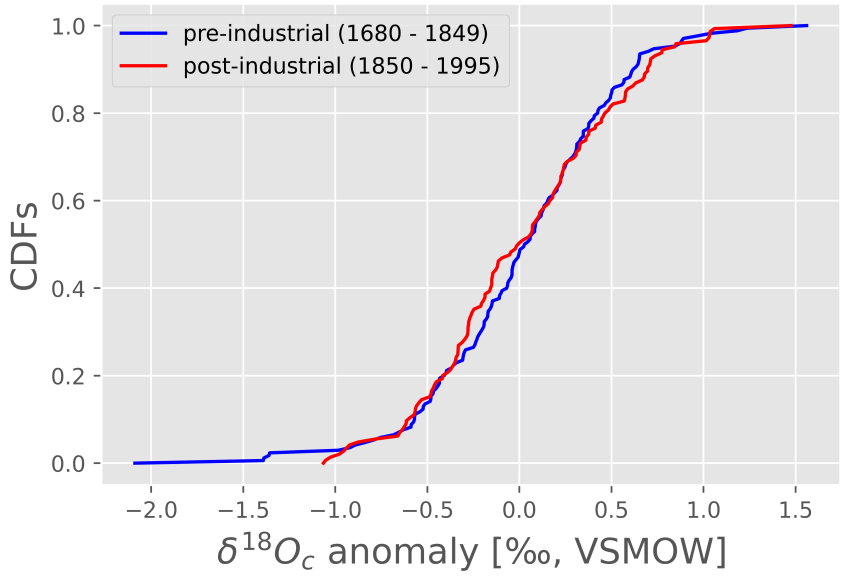

(a)

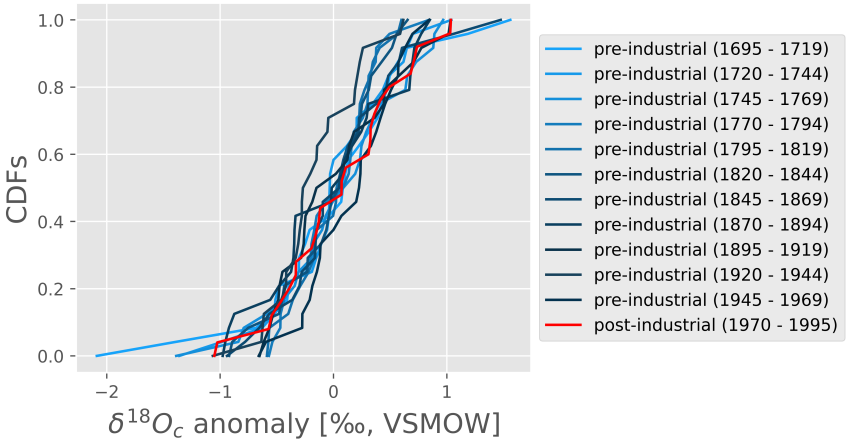

(b)

Figure A.4: Empirical cumulative probability density function (CDF) curves of the annual $\delta^{18}O_c$ variability (high-pass filtered $m = 11$). The red line shows the period after the industrial revolution, while the blue lines show the periods before the industrial revolution. We used two different definitions of the anthropogenic era to show that the results are not sensitive to its definition of the beginning of the exponential increase in the anthropogenic forcings. In (a) the industrial revolution began in 1850, while in (b) the industrial revolution began in 1970.

Bibliography

[1] E. Aldrian and R. D. Susanto. Identification of three dominant rainfall regions within Indonesia and their relationship to sea surface temperature. *International Journal of Climatology*, 23(12):1435–1452, 2003.

[2] M. R. Allen and W. J. Ingram. Constraints on future changes in climate and the hydrologic cycle. *Nature*, 419(6903):228–232, Sep 2002.

[3] K. J. Anchukaitis, M. N. Evans, T. Lange, D. R. Smith, S. W. Leavitt, and D. P. Schrag. Consequences of a rapid cellulose extraction technique for oxygen isotope and radiocarbon analyses. *Analytical Chemistry*, 80(6):2035–2041, 2008.

[4] M. Barbour, J. Roden, G. Farquhar, and J. Ehleringer. Expressing leaf water and cellulose oxygen isotope ratios as enrichment above source water reveals evidence of a Péclet effect. *Oecologia*, 138:426–35, 03 2004.

[5] E. Bauer, M. Claussen, V. Brovkin, and A. Hünerbein. Assessing climate forcings of the Earth system for the past millennium. *Geophysical Research Letter*, 30, 03 2003.

[6] H. Bellenger, E. Guilyardi, J. Leloup, M. Lengaigne, and J. Vialard. ENSO representation in climate models: From CMIP3 to CMIP5. *Climate Dynamics*, 42:1999–2018, 2014.

[7] W. Cai, S. Borlace, M. Lengaigne, P. Rensch, M. Collins, G. Vecchi, A. Timmermann, A. Santoso, M. McPhaden, L. Wu, M. England, G. Wang, E. Guilyardi, and F-F. Jin. Increasing Frequency of Extreme El Niño Events due to Greenhouse Warming. *Nature Climate Change*, 4, 01 2014.

[8] W. Cai, A. Santoso, M. Collins, B. Dewitte, C. Karamperidou, J-S. Kug, M. Lengaigne, M. J. McPhaden, M. F. Stuecker, A. S. Taschetto, et al. Changing El Niño–Southern Oscillation in a warming climate. *Nature Reviews Earth & Environment*, 2(9):628–644, 2021.

[9] W. Cai, G. Wang, A. Santoso, M. McPhaden, L. Wu, F-F. Jin, A. Timmermann, M. Collins, G. Vecchi, M. Lengaigne, M. England, D. Dommenget, K. Takahashi, and E. Guilyardi. Increased frequency of extreme La Niña events under greenhouse warming. *Nature Climate Change*, 5:132–137, 01 2015.

[10] M. Cane, A. Clement, A. Kaplan, Y. Kushnir, D. Pozdnyakov, R. Seager, S. Zebiak, and R. Murtugudde. Twentieth-Century Sea Surface Temperature Trends. *Science*, 275:957, 02 1997.

[11] M. A. Cane. Forecasting El Niño with a Geophysical Model. In M. H. Glantz, R. W. Katz, and N. Nicholls, editors, *Teleconnections Linking Worldwide Climate Anomalies.*, chapter 11, pages 345–369. Cambridge U. Press, Cambridge, England, 1991.

[12] D. Chen, M. A. Cane, A. Kaplan, S. E. Zebiak, and D. Huang. Predictability of El Niño over the past 148 years. *Nature*, 428(6984):733–736, 2004.

[13] L. Chen, T. Li, Y. Yu, and S. K. Behera. A possible explanation for the divergent projection of ENSO amplitude change under global warming. *Climate Dynamics*, 49:3799–3811, 2017.

[14] A. C. Clement, R. Seager, M. A. Cane, and S. E. Zebiak. An Ocean Dynamical Thermostat. *Journal of Climate*, 9(9):2190 – 2196, 1996.

[15] Kim M Cobb, Christopher D Charles, Hai Cheng, and R Lawrence Edwards. El Niño/Southern Oscillation and tropical Pacific climate during the last millennium. *Nature*, 424(6946):271–276, 2003.

[16] M. Collins. El Niño or La Niña-like climate change? *Clim. Dyn.*, 24:89–104, 2005. doi: 10.1007/s00382-004-0478-x.

[17] M. Collins, S. I. An, W. Cai, A. Ganachaud, E. Guilyardi, F.-F. Jin, M. Jochum, M. Lengaigne, S. Power, A. Timmermann, G. Vecchi, and A. Wittenberg. The impact of global warming on the tropical Pacific Ocean and ENSO. *Nature Geoscience*, 3:391–397, 2010. doi: 10.1038/NGEO868.

[18] David Colquhoun. An investigation of the false discovery rate and the misinterpretation of p-values. *Royal Society Open Science*, 1(3):140216, 2014.

[19] PAGES2k Consortium et al. A global multiproxy database for temperature reconstructions of the common era. *Scientific data*, 4, 2017.

[20] R. D'Arrigo, R. Wilson, J. Palmer, P. Krusic, A. Curtis, J. Sakulich, S. Bijaksana, S. Zulaikah, L. O. Ngkoimani, and A. Tudhope. The reconstructed Indonesian warm pool sea surface temperatures from tree rings and corals: Linkages to Asian monsoon drought and El Niño–Southern Oscillation. *Paleoceanography*, 21(3), 2006.

[21] S. G. Dee, K. M. Cobb, J. Emile-Geay, T. R. Ault, R. L. Edwards, H. Cheng, and C. D. Charles. No consistent ENSO response to volcanic forcing over the last millennium. *Science*, 367(6485):1477–1481, 2020.

[22] H. F. Diaz, M. P. Hoerling, and J. K. Eischeid. ENSO variability, teleconnections and climate change. *International Journal of Climatology*, 21(15):1845–1862.

[23] J. Emile-Geay, K. M. Cobb, J. E. Cole, M. Elliot, and F. Zhu. *Past ENSO Variability*, chapter 5, pages 87–118. American Geophysical Union (AGU), 2020.

[24] M. N. Evans. Toward forward modeling for paleoclimatic proxy signal calibration: A case study with oxygen isotopic composition of tropical woods. *Geochemistry, Geophysics, Geosystems*, 8(7), 2007.

[25] M. N. Evans, K. J. Selmer, B. T. Breeden III, A. S. Lopatka, and R. E. Plummer. Correction algorithm for online continuous flow δ^{13}C and δ^{18}O carbonate and cellulose stable isotope analyses. *Geochemistry, Geophysics, Geosystems*, 17(9):3580–3588, 2016.

[26] M. N. Evans, S. E. Tolwinski-Ward, D. M. Thompson, and K. J. Anchukaitis. Applications of proxy system modeling in high resolution paleoclimatology. *Quaternary science reviews*, 76:16–28, 2013.

[27] A. Gessler, J. P. Ferrio, R. Hommel, K. Treydte, R. A. Werner, and R. K. Monson. Stable isotopes in tree rings: towards a mechanistic understanding of isotope fractionation and mixing processes from the leaves to the wood. *Tree Physiology*, 34(8):796–818, 06 2014.

[28] M. Ghil, M. R. Allen, M. D. Dettinger, K. Ide, D. Kondrashov, M. E. Mann, W. Robertson, A, A. Saunders, Y. Tian, F. Varadi, et al. Advanced spectral methods for climatic time series. *Reviews of Geophysics*, 40(1):3–1, 2002.

[29] A. Giannini, A. Robertson, and J. Qian. A role for tropical tropospheric temperature adjustment to El Niño-Southern Oscillation in the seasonality of monsoonal Indonesia precipitation predictability. *Journal of Geophysical Research*, 112, 08 2007.

[30] N. Golyandina, A. Korobeynikov, and A. Zhigljavsky. *Singular Spectrum Analysis with R*. Springer, 2018.

[31] E. Guilyardi, A. Capotondi, M. Lengaigne, S. Thual, and A. Wittenberg. *ENSO Modeling: History, Progress, and Challenges*, pages 199–226. 11 2020.

[32] Eric Guilyardi. El Niño–mean state–seasonal cycle interactions in a multi-model ensemble. *Climate Dynamics*, 26:329–348, 2006.

[33] G. J. Hakim, J. Emile-Geay, E. J. Steig, D. Noone, D. M. Anderson, R. Tardif, N. Steiger, and W. A. Perkins. The last millennium climate reanalysis project: Framework and first results. *Journal of Geophysical Research: Atmospheres*, 121(12):6745–6764, 2016.

[34] J-I. Hamada, M. Yamanaka, J. Matsumoto, S. Fukao, P. Winarso, and T. Sribimawati. Spatial and Temporal Variations of the Rainy Season over Indonesia and their link to ENSO. *Journal of the Meteorological Society of Japan*, 80:285–310, 04 2002.

[35] I. Harris, P. D. Jones, T. J. Osborn, and D. H. Lister. Updated high-resolution grids of monthly climatic observations – the CRU TS3.10 Dataset. *International Journal of Climatology*, 34:623–642, 2014. doi: 10.1002/joc.3711.

[36] H. Hassani and R. Mahmoudvand. *Singular spectrum analysis: Using R*. Springer, 2018.

[37] P. Hope, B. J. Henley, J. Gergis, J. Brown, and H. Ye. Time-varying spectral characteristics of ENSO over the Last Millennium. *Climate Dynamics*, 49:1705–1727, 2017.

[38] H-Y Kao and J-Yi Yu. Contrasting Eastern-Pacific and Central-Pacific Types of ENSO. *Journal of Climate*, 22(3):615 – 632, 2009.

[39] B-H. Kim and K-J. Ha. Observed changes of global and western Pacific precipitation associated with global warming SST mode and Mega-ENSO SST mode. *Climate Dynamics*, 45, 02 2015.

[40] L. Landrum, B. L. Otto-Bliesner, E. R. Wahl, A. Conley, P. J. Lawrence, N. Rosenbloom, and H. Teng. Last Millennium Climate and Its Variability in CCSM4. *Journal of Climate*, 26(4):1085 – 1111, 2013.

[41] M. Latif and N. S. Keenlyside. El Niño/Southern Oscillation response to global warming. *Proceedings of the National Academy of Sciences*, 106(49):20578–20583, 2009.

[42] S. C. Lewis and A. N. LeGrande. Stability of ENSO and its tropical Pacific teleconnections over the last millennium. *Climate of the Past*, 11(10):1347–1360, 2015.

[43] J. Li, S-P. Xie, E. R. Cook, M. S. Morales, D. A. Christie, N. C. Johnson, F. Chen, R. D'Arrigo, A. M. Fowler, X. Gou, et al. El Niño modulations over the past seven centuries. *Nature Climate Change*, 3(9):822–826, 2013.

[44] J. Liu, B. Wang, M. A. Cane, S-Y. Yim, and J-Y. Lee. Divergent global precipitation changes induced by natural versus anthropogenic forcing. *Nature*, 493(7434):656–659, Jan 2013.

[45] Y. Liu, K. M. Cobb, H. Song, Q. Li, C-Y. Li, T. Nakatsuka, Z. An, W. Zhou, Q. Cai, J. Li, et al. Recent enhancement of central Pacific El Niño variability relative to last eight centuries. *Nature Communications*, 8(1):15386, 2017.

[46] Z. Lu, Z. Liu, J. Zhu, and K. M. Cobb. A Review of Paleo El Niño-Southern Oscillation. *Atmosphere*, 9(4):130, 2018.

[47] J. L. McBride, M. R. Haylock, and N. Nicholls. Relationships between the Maritime Continent Heat Source and the El Niño–Southern Oscillation Phenomenon. *Journal of Climate*, 16(17):2905 – 2914, 2003.

[48] W. J. Merryfield. Changes to ENSO under CO_2 doubling in a Multimodel Ensemble. *Journal of Climate*, 19(16):4009 – 4027, 2006.

[49] I. C. Nurhati, M. N. Evans, S. Y. Cahyarini, R. D. D'Arrigo, K. Y. Yoshimura, and S. H. S. Herho. δ^{18}O of marine-influenced Tectona grandis l. f. from equatorial Indonesia: A local rainfall amount and remote ENSO indicator. in preparation for submission to Paleoceanography and Paleoclimatology.

[50] J.P. Peixoto and A.H. Oort. *Physics of Climate*. American Institute of Physics, New York, 1991.

[51] N. Pumijumnong, P. Payomrat, S. Buajan, A. Bräuning, C. Muangsong, U. Chareonwong, P. Songtrirat, K. Palakit, Y. Liu, and Q. Li. Teak Tree-Ring Cellulose δ^{13}C, δ^{18}O, and Tree-Ring Width from Northwestern Thailand Capture Different Aspects of Asian Monsoon Variability. *Atmosphere*, 12(6), 2021.

[52] C. S. Ramage. ROLE OF A TROPICAL "MARITIME CONTINENT" IN THE ATMOSPHERIC CIRCULATION. *Monthly Weather Review*, 96(6):365 – 370, 1968.

[53] B. Rein, A. Lückge, L. Reinhardt, F. Sirocko, A. Wolf, and W-C. Dullo. El Niño variability off Peru during the last 20,000 years. *Paleoceanography*, 20(4), 2005.

[54] A. Robertson, V. Moron, J. Qian, C-P. Chang, F. Tangang, E. Aldrian, T. Koh, and L. Juneng. *The Maritime Continent monsoon*, pages 85–98. 04 2011.

[55] M. Rodriguez-Caton, L. Andreu-Hayles, V. Daux, M. Vuille, A. M. Varuolo-Clarke, R. Oelkers, D. A. Christie, R. D'Arrigo, M. S. Morales, M. Palat Rao, A. M. Srur, F. Vimeux, and R. Villalba. Hydroclimate and ENSO Variability Recorded by Oxygen Isotopes From Tree Rings in the South American Altiplano. *Geophysical Research Letters*, 49(4):e2021GL095883, 2022. e2021GL095883 2021GL095883.

[56] G. T. Rustic, A. Koutavas, T. M. Marchitto, and B. K. Linsley. Dynamical excitation of the tropical Pacific Ocean and ENSO variability by Little Ice Age cooling. *Science*, 350(6267):1537–1541, 2015.

[57] D. H. Schoellhamer. Singular spectrum analysis for time series with missing data. *Geophysical Research Letters*, 28(16):3187–3190, 2001.

[58] K. Schollaen, I. Heinrich, B. Neuwirth, P. J. Krusic, R. D. D'Arrigo, O. Karyanto, and G. Helle. Multiple tree-ring chronologies (ring width, δ^{13}C and δ^{18}O) reveal dry and rainy season signals of rainfall in Indonesia. *Quaternary Science Reviews*, 73:170–181, 2013.

[59] S. Stevenson, A. Capotondi, J. Fasullo, and B. Otto-Bliesner. Forced changes to twentieth century ENSO diversity in a last millennium context. *Climate Dynamics*, 52:7359–7374, 2019.

[60] A. S. Taschetto, C. C. Ummenhofer, M. F. Stuecker, D. Dommenget, Karumuri A., R. R. Rodrigues, and S-W. Yeh. *ENSO Atmospheric Teleconnections*, chapter 14, pages 309–335. American Geophysical Union (AGU), 2020.

[61] R. Vautard and M. Ghil. Singular spectrum analysis in nonlinear dynamics, with applications to paleoclimatic time series. *Physica D: Nonlinear Phenomena*, 35(3):395–424, 1989.

[62] G. A. Vecchi and B. J. Soden. Global Warming and the Weakening of the Tropical Circulation. *Journal of Climate*, 20(17):4316 – 4340, 2007.

[63] G. A. Vecchi, B. J. Soden, A. T. Wittenberg, I. M. Held, A. Leetmaa, and M. J. Harrison. Weakening of tropical Pacific atmospheric circulation due to anthropogenic forcing. *Nature*, 441(7089):73–76, 2006.

[64] P. Virtanen, R. Gommers, T. E. Oliphant, M. Haberland, T. Reddy, D. Cournapeau, E. Burovski, P. Peterson, W. Weckesser, J. Bright, S. J. van der Walt, M. Brett, J. Wilson, K. J. Millman, N. Mayorov, A. R. J. Nelson, E. Jones, R. Kern, E. Larson, C. J. Carey, İ. Polat, Y. Feng, E. W. Moore, J. VanderPlas, D. Laxalde, J. Perktold, R. Cimrman, I. Henriksen, E. A. Quintero, C. R. Harris, A. M. Archibald, A. H. Ribeiro, F. Pedregosa, P. van Mulbregt, and SciPy 1.0 Contributors. SciPy 1.0: Fundamental Algorithms for Scientific Computing in Python. *Nature Methods*, 17:261–272, 2020.

[65] R. E. Walpole, R. H. Myers, S. L. Myers, and K. Ye. *Probability and Statistics for Engineers and Scientists*, volume 5. Macmillan New York, 1993.

[66] J. Wang, J. Emile-Geay, D. Guillot, J. E. Smerdon, and B. Rajaratnam. Evaluating climate field reconstruction techniques using improved emulations of real-world conditions. *Climate of the Past*, 10(1):1–19, 2014.

[67] D. S. Wilks. *Statistical Methods in the Atmospheric Sciences*, volume 100. Academic Press, 2011.

[68] C. Xu, M. Sano, and T. Nakatsuka. Tree ring cellulose δ^{18}O of Fokienia hodginsii in northern Laos: A promising proxy to reconstruct ENSO? *Journal of Geophysical Research: Atmospheres*, 116(D24), 2011.

[69] S-W. Yeh, J-S. Kug, B. Dewitte, M-H. Kwon, B. P. Kirtman, and F-F. Jin. El Niño in a changing climate. *Nature*, 461(7263):511–514, 2009.

[70] S. Yoden, S. Otsuka, N. J. Trilaksono, and T. W. Hadi. *Recent Progress in Research on the Maritime Continent Monsoon*, chapter 6, pages 63–77. 2017.

[71] K. Yoshimura, M. Kanamitsu, D. Noone, and T. Oki. Historical isotope simulation using Reanalysis atmospheric data. *Journal of Geophysical Research: Atmospheres*, 113(D19), 2008.

[72] Z. Zhongming, L. Linong, Y. Xiaona, L. Wei, et al. AR6 Climate Change 2021: The Physical Science Basis. 2021.

[73] F. Zhu, J. Emile-Geay, K. J. Anchukaitis, G. J. Hakim, A. T. Wittenberg, M. S. Morales, M. Toohey, and J. King. A re-appraisal of the ENSO response to volcanism with paleoclimate data assimilation. *Nature Communications*, 13(1):747, 2022.

[74] F. Zhu, J. Emile-Geay, G. J. Hakim, R. Tardif, and A. Perkins. LMR Turbo (LMRt): a lightweight implementation of the LMR framework, 2021.

[75] M. Zhu, L. Stott, B. Buckley, K. Yoshimura, and K. Ra. Indo-Pacific Warm Pool convection and ENSO since 1867 derived from Cambodian pine tree cellulose oxygen isotopes. *Journal of Geophysical Research: Atmospheres*, 117(D11), 2012.